nature nanotechnology

ARTICLES

https://doi.org/10.1038/s41565-017-0024-8

Excitonic pathway to photoinduced magnetism in colloidal nanocrystals with nonmagnetic dopants

Valerio Pinchetti[1], Qiumei Di[2], Monica Lorenzon[1], Andrea Camellini[3], Mauro Fasoli[1], Margherita Zavelani-Rossi[4], Francesco Meinardi[1], Jiatao Zhang[2]*, Scott A. Crooker[5] and Sergio Brovelli[1]*

Electronic doping of colloidal semiconductor nanostructures holds promise for future device concepts in optoelectronic and spin-based technologies. Ag^+ is an emerging electronic dopant in III–V and II–VI nanostructures, introducing intragap electronic states optically coupled to the host conduction band. With its full 4*d* shell Ag^+ is nonmagnetic, and the dopant-related luminescence is ascribed to decay of the conduction-band electron following transfer of the photoexcited hole to Ag^+. This optical activation process and the associated modification of the electronic configuration of Ag^+ remain unclear. Here, we trace a comprehensive picture of the excitonic process in Ag-doped CdSe nanocrystals and demonstrate that, in contrast to expectations, capture of the photohole leads to conversion of Ag^+ to paramagnetic Ag^{2+}. The process of exciton recombination is thus inextricably tied to photoinduced magnetism. Accordingly, we observe strong optically activated magnetism and diluted magnetic semiconductor behaviour, demonstrating that optically switchable magnetic nanomaterials can be obtained by exploiting excitonic processes involving nonmagnetic impurities.

Colloidal semiconductor nanocrystals (NCs), owing to their tunable electronic properties and solution processability[1], are receiving increasing attention in the fields of optoelectronics and photonics[2–6]. In addition to size-control and heterostructuring[1] providing spectral tunability and control over the exciton dynamics, the insertion of tiny amounts of transition metal ions (doping[7,8]) is an effective strategy for achieving broadband Stokes-shifted luminescence[8–10], enhanced electrical transport[11,12] and tailored magnetic behaviours arising from the *sp*–*d* spin-exchange interaction between the NC quantized states and the *d* electrons of the impurity atom[9,13,14]. The doping of chalcogenide NCs with Mn has been investigated extensively[9] for applications in spin-based electronics[15,16]. Because Mn^{2+} ions are isovalent to the lattice cations, their substitutional incorporation in II–VI NCs introduces no additional charge into the system. For small, wide-bandgap CdSe NCs (energy gap, $E_g > 2.1$ eV), the Mn *d* states behave as radiative recombination centres for band-edge excitons, resulting in the typical Mn^{2+} luminescence at ~2.1 eV sensitized by the host particle[9], whereas for larger NCs ($E_g < 2.1$ eV), the unpaired electronic spins of the Mn ions interact with photogenerated[17] and electrically injected[18] excitons to form magnetic polarons. Conversely, Cu and Ag ions introduce a single intragap deep acceptor level close to the host valence band (VB)[19–22], which radiatively captures a conduction band (CB) electron[10,11,23,24], making the dopant-related emission subject to quantum confinement and heterostructuring[23]. Being aliovalent with respect to cations in II–VI and III–V semiconductors, their insertion changes the overall charge within the host compound, resulting in p- or n- type doping depending on their coordination state[11,12,23–26]. For this reason, they are commonly termed 'electronic dopants'. In the case of Ag-doped NCs, electrical transport measurements on Ag:CdSe NCs have shown that, in the low doping regime (<1%), Ag atoms incorporate as interstitial impurities, whereas for higher doping levels they occupy substitutional cation sites, respectively leading to n- or p-type transport[11,27]. In ref. [12], p-type transport in field-effect transistors incorporating PbSe NCs with high Ag doping levels was consistently observed, and scanning tunnelling spectroscopy[26] showed the Fermi level (FL) of heavily doped Ag:InAs NCs close to the VB onset. Recent theoretical calculations of Ag:CdSe NCs (3.9% Ag) predicted a deep acceptor state close to the NC VB with optical behaviour similar to the acceptor state in NCs with Cu^+ impurities, yet with a more pronounced *s* character deriving from the coordinating Se anions[24].

Despite Ag and Cu belonging to the same group of the periodic table, their electronic properties show fundamental differences arising from the interplay between their second ionization (IE_2) and crystal field stabilization energies. In the case of Cu (atomic radius $r_0 = 1.35$ Å), the enhanced stability due to tetragonal distortion of the local environment of Cu^{2+} compensates the energy required to form a doubly-charged ion ($IE_2^{Cu} = 20.29$ eV)[28]. This results in the amphoteric character of Cu dopants, which exhibit stable oxidation states +1 or +2 depending on the position of the Fermi energy[10,21,22]. Conversely, Ag is energetically less sensitive to the breakdown of local symmetry due to its ~20% larger atomic radius (1.60 Å) with respect to Cu, making its crystal field stabilization energy typically insufficient to counterbalance its larger second ionization energy ($IE_2^{Ag} = 21.45$ eV)[28–31]. As a result, Ag cations assume the +1 oxidation state almost exclusively, whereas the stable +2 configuration is found in rare compounds where Ag^{2+} ions are protected against reduction by suitable ligands[28,32]. Consistently, in bulk metal chalcogenides, Ag atoms are inserted as nonmagnetic +1 impurities[33] with electronic configuration $[Kr]4d^{10}$, often coupled to a compensating defect ensuring charge neutrality[19,34]. Having a full *d* shell,

---

[1]Dipartimento di Scienza dei Materiali, Università degli Studi di Milano-Bicocca, Milano, Italy. [2]Beijing Key Laboratory of Construction Tailorable Advanced Functional Materials and Green Applications, School of Materials Science and Engineering, Beijing Institute of Technology, Beijing, China. [3]Dipartimento di Fisica, Politecnico di Milano, Milano, Italy. [4]Dipartimento di Energia, Politecnico di Milano and IFN-CNR, Milano, Italy. [5]National High Magnetic Field Laboratory, Los Alamos, NM, USA. *e-mail: zhangjt@bit.edu.cn; sergio.brovelli@unimib.it

luminescence in Ag-doped systems requires transfer of the photoexcited hole from the host VB to the Ag^+ site, which then behaves as a radiative acceptor centre for a CB electron[24,29,34,35]. Similarly, Cu^+ centres are not magnetic (there is no unpaired electron spin in their full 3*d* shell) and are optically passive; capture of a VB hole is necessary to promote them to Cu^{2+} (with electron-accepting capability) and thereby activate the Cu-related luminescence[10,36]. For lower Fermi energies, the oxidation state of Cu becomes +2 (electronic configuration $[Ar]3d^9$): The 3*d* shell now contains one unpaired electron and therefore exhibits paramagnetic character and hole-like behaviour, resulting in the characteristic Cu luminescence without the explicit need for a photogenerated VB hole[22,23]. Spectroelectrochemistry (SEC) experiments[10] have indicated that the emission efficiency of Cu-doped NCs is unaffected by trapping of the VB hole, suggesting a dominant role of substitutional Cu^{2+} centres in the emission process. In support of this picture, magnetic circular dichroism (MCD) studies on the same Cu:ZnSe NCs revealed enhanced and strongly temperature-dependent Zeeman splitting of the 1S exciton, indicating *sp*–*d* exchange coupling between the 1S exciton and paramagnetic spins in the NC—a defining characteristic of diluted magnetic semiconductors (DMSs)[14]. The paramagnetism of Cu-doped NCs was observed to be intensified by ultraviolet (UV) illumination. This was ascribed to localization of the VB hole at the nonmagnetic Cu^+, making it formally Cu^{2+}-like and thereby increasing the number of paramagnetic centres in a NC[14].

This result brought into focus the idea that optically switchable magnetism can be achieved by exploiting excitonic mechanisms in nanostructures that are doped with nominally nonmagnetic dopants, such as Ag. This concept has not yet been realized, and a comprehensive picture of the photophysical and magnetic phenomena in Ag-doped NCs is still lacking. In this work, we aim to address this by combining photoluminescence (PL) and transient transmission (TT) measurements with SEC methods and MCD spectroscopy on Ag-doped CdSe NCs.

Synthesis and optical properties of Ag:CdSe NCs

Ag-doped CdSe NCs (3% Ag) were prepared according to the procedure described in the Methods[25]. The compositional and structural details of the NCs are described in Supplementary Figs. 1–3 and Supplementary Table 1, showing spherical particles with an average radius of 2.2 ± 0.4 nm in a wurtzite crystal structure.

The absorption and PL spectra of Ag:CdSe NCs (Fig. 1a) show the 1S absorption peak of the CdSe host at ~2.11 eV, resonant with a weak band-edge emission (BE-PL) at ~2.05 eV with an average lifetime of ~11 ns (Fig. 1b), probably arising from a minor subpopulation of NCs in which transfer of the photohole to the Ag^+ centre is less efficient than BE exciton decay. The absorption and emission spectra of undoped NCs are presented in Supplementary Fig. 4, and show that the 1S exciton energy is not affected by Ag. The emission spectrum of Ag:CdSe NCs is dominated by a broadband component at ~1.66 eV with an average lifetime of ~220 ns due to the radiative decay of CB electrons to the localized intragap states of Ag (Ag^+-PL), Stokes-shifted by ~400 meV from the 1S absorption peak[24,25]. Notably, the absorption spectrum shows a broad low-energy component extending to 1.7 eV, nearly resonant with the Ag^+-PL band. By tuning the excitation energy from 3.0 eV (above the CdSe bandgap) down to 1.8 eV (below the NC band-edge), Ag^+-PL is still observed (Fig. 1c). This indicates that the *d* electrons of Ag^+ can be promoted to the NC CB by direct optical excitation, following the reaction $Ag(d^{10}) + h\nu \rightarrow Ag(d^9) + e_{CB}$ ($h\nu$ is the photon energy and e_{CB} indicates an electron in the CB) where Ag^+ species are temporarily photoconverted into Ag^{2+}. As a result, the PL excitation (PLE) spectrum of the 1.65 eV emission shown in the inset of Fig. 1a resembles well the absorption profile down to subbandgap energies.

Independent confirmation of the proposed mechanism is provided by the TT spectra under BE excitation and intragap pumping of Ag^+, as shown in Fig. 1d. Band-edge pumping results in the typical TT spectrum of CdSe NCs, with an intense positive band at ~2.15 eV corresponding to bleaching of the 1S absorption due to state filling of the double-degenerate CB (Supplementary Fig. 5)[1]. Importantly, the TT spectrum shows an additional positive band resonant with the Ag^+ absorption at 1.9 eV, indicating that the transition of Ag^+ centres is bleached by BE pumping. Under intragap pumping of Ag^+ at 1.95 eV, in addition to the Ag^+ bleaching, we observe photobleaching of the 1S absorption. Both effects confirm that direct excitation of Ag^+ promotes its *d* electron to the NC CB, leading to photobleaching by state filling. Inspection of the time transients of the bleaching signals in Fig. 1e enables us to measure the hole localization time from the NC VB to the Ag^+. Under BE pumping at 2.3 eV, the 1S bleaching growth is instantaneous with a rise time below the resolution limit of our apparatus (~100 fs), whereas the Ag^+ bleaching rise shows a slower component with a time constant of ~1.4 ps (Supplementary Fig. 7). By contrast, under direct Ag^+ excitation at 1.95 eV (Fig. 1e, inset), the Ag^+ bleaching growth is instantaneous. Thus, the difference in the bleaching signals is related to hole dynamics; in particular, under BE excitation the slow rise time describes migration of the photohole from the NC VB to the Ag^+, similar to the hole localization observed in CdSe/CdS core–shell structures with shell excitation[37].

Spectroelectrochemistry experiments

To confirm the above mechanism and to clarify the nature of the intragap dopant state, we conducted SEC experiments. The experimental set-up is presented in Fig. 2a, which also shows a schematic depiction of the NC band structure featuring the fully occupied *d* state of Ag^+ in the lower part of the energy gap. In unperturbed conditions, the FL is located between the Ag^+ level and the CB of the NC host. The intragap defect states responsible for the SEC behaviour are located in energy above the FL, in agreement with the electrochemical (EC) response described later in this section. The NCs are continuously excited and PL is collected under the application of an EC potential (V_{EC}) that tunes the position of the FL[10,38]: negative V_{EC} raises the Fermi energy and leads to passivation of electron traps. Concomitantly, excess electrons accumulating in surface defects become efficient traps for photogenerated holes. Conversely, positive V_{EC} (corresponding to lowering the FL) depletes the NC of photoexcited electrons and passivates hole-trapping states. The brightening versus quenching effect of V_{EC} on the NC emission is therefore determined by competition between the passivation and activation of carrier traps, by the respective trapping rates and by the occupancy of the surface states under unperturbed conditions.

Figure 2b presents the complete set of PL spectra of the NCs under application of negative V_{EC}. The evolution of the integrated intensity of the BE-PL and Ag^+-PL during the scan is shown in Fig. 2c. For $|V_{EC}| < 1.2$ V, no effect is observed. This is in agreement with previous SEC results using indium tin oxide (ITO)/ZnO substrates and is due to the effect of the dielectric ligands and the potential drop across the ZnO layer[10,39,40]. At $|V_{EC}| \geq 1.2$ V, both PL intensities undergo a sudden drop, reaching ~40% dimming at $V_{EC} = -2.5$ V. For both emissions, when returning back to $V_{EC} = 0$ V, the PL intensity increases, resulting in ~90% recovery of the original intensity. The PL brightening is markedly slower than the respective drop and also proceeds over time when no potential is applied. To investigate this aspect in deeper detail, we performed an on/off scan in which the PL was monitored continuously while the potential, initially set to $V_{EC} = 0$ V, was raised to −2.5 V, kept constant for 30 s, then brought back to 0 V. The BE-PL and Ag^+-PL intensities during the scan are presented in Fig. 2d, which shows the sudden drop of both bands with applied negative V_{EC}, followed by a slow recovery that proceeds over time for ~15 min. This indicates that the potential

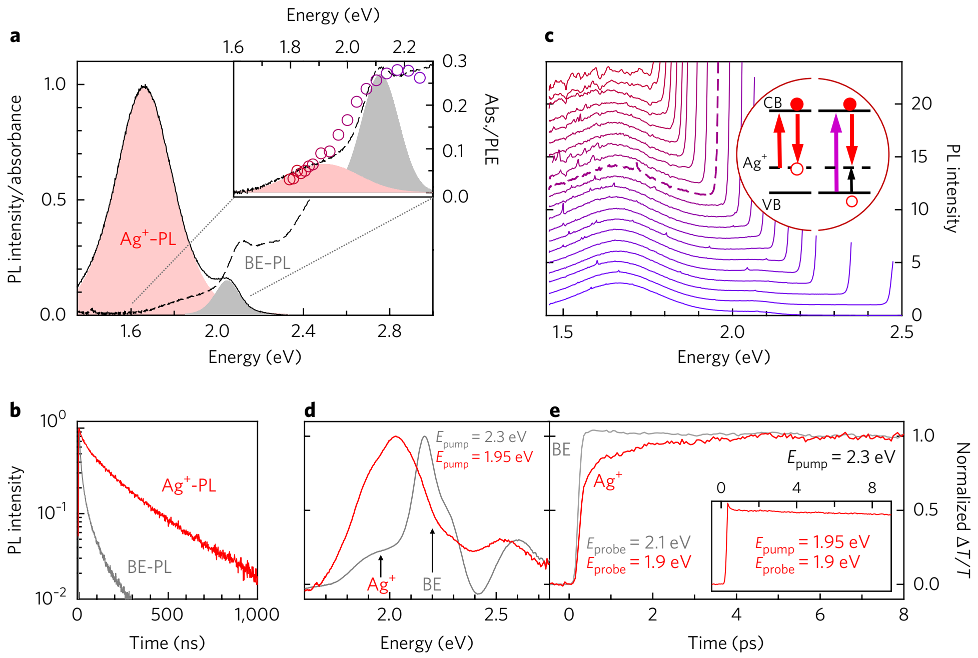

Fig. 1 | Optical properties of Ag-doped CdSe NCs. **a**, Optical absorption (dashed line) and PL spectra of Ag-doped CdSe NCs (radius 2.2 ± 0.4 nm, pulsed excitation at 3.1 eV, 500 kHz repetition rate, 100 nJ cm^{-2}, 2 s acquisition time) in toluene showing the band-edge PL band (shaded grey) and dopant-related emission (shaded red). Inset: enlargement of the 1.6–2.25 eV region emphasizing the intragap absorption band peaked at ~1.9 eV due to subbandgap absorption by Ag^+ impurities (red shading) on the low-energy side of the 1S feature at ~2.1 eV (grey shading). Circles represent the PLE spectrum of the Ag^+-PL at ~1.65 eV. **b**, Normalized PL decay curves of BE-PL and Ag^+-PL measured at 2.05 eV and 1.66 eV (bandwidth of ~20 meV) using 3.1 eV excitation. **c**, PL spectra of the same NCs under progressively lower energy excitation (from bottom to top). The colour scheme is the same as the circles in the inset of **a**. A portion of the excitation light is included for reference. This allows for direct comparison between the different measurements. The dashed line roughly indicates the transition between above-gap and below-gap excitation depicted in the right- and left-hand side of the scheme shown in the inset. **d**, Normalized transient transmission spectra after band-to-band pumping at 2.3 eV (grey curve) and intragap excitation of Ag^+ at 1.95 eV (red curve). Spectra are collected after 1.5 ps delay, and in both cases the fluence is set to excite an average of 0.1 excitons per NC. The corresponding raw data are provided in Supplementary Fig. 6. The black arrows indicate the BE and Ag^+ bleaching contributions. **e**, Normalized bleaching $\Delta T/T$ kinetics at 1S absorption (2.1 eV, grey line) and Ag^+ absorption (1.9 eV, red line) after pumping close to the band-edge at 2.3 eV to avoid thermalization effects. Bleaching of the 1S absorption is instantaneous, whereas the Ag^+ signal shows a longer rise time due to transfer of the photohole from the VB to Ag^+. Inset: Kinetics of the Ag^+ bleaching becomes instantaneous upon direct pumping at 1.95 eV. The fast component at early delay times is due to interference effects. All measurements were performed at room temperature.

sweep causes no damage to the NC surfaces, as confirmed in Supplementary Fig. 8 and by inspection of PL spectra collected for different V_{EC} values (Fig. 2e), which show identical emission profiles under all EC conditions. The SEC response is therefore ascribed to reversible activation/passivation of traps, probably associated with under-coordinated surface atoms or dangling bonds. Specifically, the observed drop of the PL intensity suggests that nonradiative trapping of holes in activated defects is not counterbalanced by the concomitant PL brightening effect of suppressed electron trapping. The slow PL recovery at $V_{EC} = 0$ V, in turn, suggests slow detrapping of trapped holes, in agreement with the long discharging time found in IV–VI NCs[41]. We notice that the PL recovery is unaffected by illumination and occurs nearly identically under continuous or intermittent excitation condition (Supplementary Fig. 9). The similar SEC responses of the BE-PL and Ag^+ emission indicate that the intrinsic and dopant-related decay pathways are equally quenched by hole trapping, which confirms the picture of the dopant-related emission requiring localization of a VB hole in the Ag^+ site to activate its capability to accept a CB electron. SEC measurements performed under intragap excitation of the Ag^+-PL are reported and discussed in Supplementary Fig. 10.

The results of the SEC measurements under positive potentials are reported in Fig. 2f, and show no variation in either the BE-PL or Ag^+-PL for V_{EC} up to 1.5 V. Because these NCs are not passivated with a wide-energy-gap shell that suppresses electron trapping, the absence of quenching by positive V_{EC} points to a situation in which defect states are positioned in energy just above the FL; that is, they are already devoid of electrons at $V_{EC} = 0$ V (Fig. 2a). As a result, similar to what has been observed in perovskite NCs[39], their occupancy cannot be further reduced by positive V_{EC}, which makes the PL insensitive to oxidative potentials. This also explains the absence of a PL brightening effect due to suppressed hole trapping by EC removal of excess electrons in NC surface states, and indicates that, under unperturbed conditions, electron trapping is the main feature responsible for nonradiative losses in our NCs (PL quantum yield Φ_{PL} of ~5%). Finally, the position of the localized states deep inside the NC energy gap is in agreement with the observed minutes-long detrapping time of trapped holes at $V_{EC} = 0$ V, leading to the asymmetry between the dimming and brightening kinetics (Fig. 2c,d).

Magnetic circular dichroism measurements

One important consequence of the recombination mechanism emerging from the spectroscopic measurements is that the optical activity (that is, the electron-accepting capability) of the dopant site depends on the transient excitation of Ag^+ from its $4d^{10}$ ground-state configuration with nonmagnetic character to the $4d^9$ state with paramagnetic behaviour. An analogous process underpins the optical excitation of Cu^+-doped NCs, leading to the formation of paramagnetic Cu^{2+} centres whose unpaired electron gives rise to strong *sp–d* spin exchange with the 1S exciton[14]. In Ag-doped NCs, because

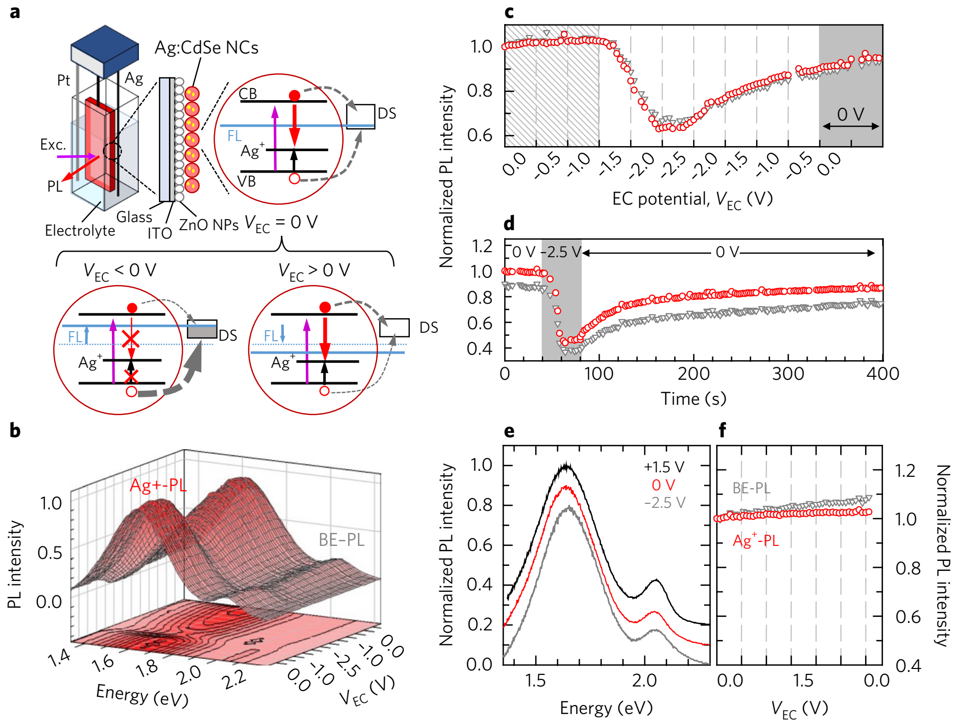

Fig. 2 | SEC of Ag:CdSe NCs. a, Schematic of the SEC set-up consisting of an EC cell with $TBAClO_4$ in propylene carbonate (0.1 M) as an electrolyte and a working electrode comprising an ITO-coated glass slide covered with a layer of ZnO nanoparticles (NPs) and Ag:CdSe NCs. Also shown is the radiative recombination pathway (red arrow) of photoexcited CB electrons to the intragap Ag state following capture of the VB hole (black arrow). Competitive nonradiative carrier trapping processes to defect states (DSs) are shown as grey dashed arrows. The effect of the EC potential on PL intensity depends on the filling/emptying DSs (right of the band diagram) in response to changes in the position of the FL (blue line). **b**, A series of PL spectra (0.5 s acquisition time per frame) for a stepwise scan of the EC potential from 0 V to −2.5 V and then back to 0 V (100 mV steps, each lasting 10 s). **c**, Spectrally integrated intensity of the BE- and Ag^+-PL bands (grey triangles and red circles respectively) as a function of V_{EC} extracted from the spectra in **b**. The patterned area for $|V_{EC}| \leq 1$ V highlights the regime in which the interlayer ZnO NPs and the dielectric ligands attenuate the effect of the applied potential. The grey shaded portion emphasizes PL growth over time at $V_{EC} = 0$ V. **d**, Intensity of the BE- and Ag^+-PL bands (grey triangles and red circles, respectively) for excitation at 3.1 eV during on/off voltage cycles for the negative electrochemical potential ($V_{EC} = 0$, −2.5, 0 V) showing recovery of the initial intensity due to slow release of trapped holes. **e**, Normalized PL spectra at $V_{EC} = 0$ V (red line), −2.5 V (grey line) and +1.5 V (black line). Spectra are shifted vertically for clarity. **f**, Spectrally integrated PL intensity during a stepwise scan of the EC potential to positive values (100 mV steps, each lasting 10 s). All intensities in **c**, **d** and **f** are normalized to their values at $V_{EC} = 0$ V. All measurements were conducted using 3.1 eV excitation with fluence of 100 nJ cm^{-2}.

of the large second ionization energy of Ag not being compensated by the local lattice distortion, this behaviour would be somewhat unexpected. On the other hand, an experimental observation of *sp–d* exchange between the NC bands and any unpaired *d* electrons of Ag, would unambiguously indicate that capture of the VB hole leads to a metastable Ag^{2+}-like excited state in CdSe NCs and would demonstrate that DMS physics can be triggered optically in NCs with nonmagnetic dopants.

To address this, we performed MCD experiments as a function of temperature and magnetic field *B*. Figure 3a presents the MCD spectra of Ag:CdSe NCs at increasing magnetic field up to $B = 7$ T at 3 K, together with the corresponding linear absorption spectrum (dashed black line). The MCD spectra show two main peaks at ~2.15 eV and ~2.6 eV, corresponding to the NC 1S and 2S exciton absorption peaks and a minor contribution at 1.9 eV due to direct absorption by the Ag^+ dopants. The magnetic response of the 1S absorption peak shows intensification with increasing *B* and decreasing temperature (Fig. 3b), revealing a strong paramagnetic response. We stress that the temperature dependence of the MCD is the most direct and arguably only definitive indication of the presence of coupling between carriers in the NC bands and paramagnetic species[14,15]. The data in Fig. 3 are therefore unambiguous signatures of *sp–d* exchange due to progressive alignment of the photoexcited Ag^{2+} spins to the magnetic field. This provides the first demonstration of photoinduced DMS physics in Ag-doped NCs[42]. To quantify this effect, we extracted the Zeeman splitting energy ΔE_Z of the 1S exciton as a function of *B* and temperature. Figure 3c presents the evolution of ΔE_Z when continuously increasing *B* from 0 to 7 T in the 1.85–40 K temperature range. In agreement with Fig. 3a,b, ΔE_Z is markedly temperature-dependent and shows clear saturation for $T < 5$ K. This is supported by the fitting of ΔE_Z with the Brillouin functional form for DMS materials[42]:

$$\Delta E_Z = g_{ex}\mu_B B + \Delta E_{sp-d} B_J\left(\frac{g_{Ag}\mu_B J B}{k_B T}\right) \qquad (1)$$

where the first term is the linear and temperature-independent Zeeman splitting arising from the intrinsic Landé factor of the CdSe exciton (g_{ex})[43] and the second term accounts for any additional splitting due to the *sp–d* exchange interaction between the semiconductor bands and dopant spins[42]. The magnitude of the *sp–d* splitting energy, ΔE_{sp-d}, is weighted by the average spin projection along *B*, which is modelled by the Brillouin function $B_J\left(g_{Ag}\mu_B J B / k_B T\right)$, describing the magnetic field- and temperature-dependent paramagnetism of the ions with spin *J*. Here, g_{Ag} is the Ag^{2+} *g* factor, μ_B is the Bohr magneton, and k_B is the Boltzmann constant. For d^9 dopants in II–VI compounds[44,45], the tetragonal crystal field lowers and

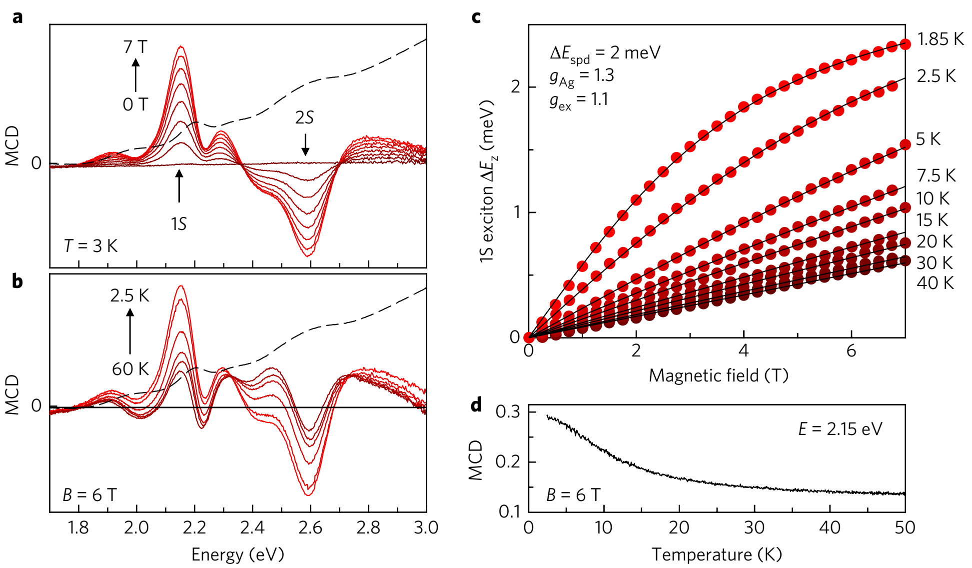

Fig. 3 | DMS physics in Ag-doped NCs. a, MCD spectra of Ag:CdSe NCs, from which the Zeeman splitting of the 1S exciton can be inferred. MCD spectra are shown at 3 K in different magnetic fields from 0 to 7 T. **b**, MCD spectra at 6 T, at temperatures from 60 to 2.5 K. The linear absorption spectrum is reported as a dashed black line in **a** and **b**. **c**, Enhanced Zeeman splitting of the 1S band-edge exciton versus magnetic field, at various temperatures. The high field saturation and strong temperature dependence indicate the existence of *sp*–*d* exchange coupling between the conduction/valence bands of the semiconductor host and a paramagnetic species in the NCs. This species is probably Ag dopants excited by fast localization (capture) of the VB hole. Lines are fits to a Brillouin function using a single set of parameters. **d**, Intensity of the MCD signal of the 1S exciton at 6 T as a function of temperature from 2.5 to 50 K.

increases the energy of the sixfold degenerate t_{2g} states and the fourfold degenerate e_g states, respectively. We therefore use $J=1/2$ for the lowest Kramer doublet to fit the experimental data with equation (1), setting as shared parameters the *sp*–*d* exchange interaction and the exciton and dopant Landé factors. The best fit for the whole set of data in Fig. 3c was obtained using $\Delta E_{sp\text{-}d}=2.0$ meV, $g_{ex}=1.1$ and $g_{Ag}=1.3$. The obtained g_{ex} is comparable to the values reported for undoped[43,46,47] and Cu-doped CdSe NCs[48], and g_{Ag} is consistent with Ag-doped bulk ZnSe showing a magnetic response that was suggested to originate from a photoexcited $[\mathrm{Ag_{Zn}}^{2+}\text{–}\mathrm{Se}^{2-}\text{–}\mathrm{Ag_i}^{+}]^{+}$ paramagnetic acceptor complex involving a substitutional and an interstitial Ag ion[49]. The effect of temperature on the MCD intensity at the 1S absorption energy is quantified in Fig. 3d, confirming the strong paramagnetic response below $T=20$ K. The approximate estimation of the net exchange constants is reported in the Supplementary Discussion.

Photoinduced paramagnetism in Ag:CdSe NCs

We stress that the observed magnetic behaviour in Ag:CdSe NCs is not a ground-state property, but a photoinduced effect due to the probe light used for MCD measurements that necessarily matches the absorption spectrum of the NCs. This is highlighted in Fig. 4a,b, which shows the linear growth of the MCD signal with increasing probe intensity. This behaviour is unusual because the MCD signal is an intrinsically normalized physical quantity corresponding to the ratio between the absorption difference of right and left circularly polarized light and the intensity of the transmitted portion of the light probe. The amplitude of the MCD signal for conventional magnetic materials is thus independent of the intensity of the probe beam. Conversely, the observed strong dependence of the MCD amplitude on the probe intensity is a direct consequence of the particular physics of Ag^+ dopants in CdSe NCs. To investigate this, we performed MCD spectroscopy at $B=6$ T in the presence and absence of additional 3.1 eV laser excitation. Remarkably, as shown in Fig. 4c, the MCD signal increases by up to ~100% with additional UV illumination, without any spectral modification. The effect is emphasized in Fig. 4d, which shows the MCD signal of the 1S absorption peak during a magnetic field ramp, with and without UV illumination, confirming, in both cases, the strongly nonlinear field dependence characteristic of *sp*–*d* exchange. With the exception of the low-field region (<2 T), both trends are well described by equation (1), using appropriate scaling of $\Delta E_{sp\text{-}d}$ to account for the larger number of photoactivated paramagnetic impurities in the sample.

To gather deeper insights into the effect of photoexcitation on the magnetic response of Ag:CdSe NCs and to identify correlations with the exciton recombination mechanism emerging from the SEC results, we monitored the evolution of the photoinduced MCD over time as a function of the UV excitation fluence. As shown in Fig. 4e, increasing the fluence of the UV light leads to faster MCD growth and higher maximum values, confirming the direct relationship between the magnetization and NC excitation. At all adopted UV excitation fluence values, the NCs are well within the single exciton regime and thus only one Ag^+ centre per NC is photoconverted to Ag^{2+}. Accordingly, the intensification of the MCD signal with increasing UV excitation power is due to the larger number of photoexcited NCs in the ensemble. For all fluences used, when the UV laser is turned off, the MCD signal decreases very slowly over several minutes. Such minutes-long persistence of the metastable paramagnetic state, extending over nine orders of magnitude longer than the dopant emission lifetime (~220 ns), indicates that radiative decay of the CB electron in the Ag state is not the determining process in the $\mathrm{Ag}^{2+}\rightarrow\mathrm{Ag}^{+}$ dynamics responsible for the drop of the photoinduced MCD. This effect can be explained by the presence of localized states positioned in energy above the NC Fermi energy efficiently trapping CB electrons, as indicated by SEC in Fig. 2. As a result of electron trapping, the lifetime of the metastable paramagnetic state would be dramatically extended with respect to the corresponding PL decay, and the MCD recovery time would be dictated by the electron detrapping dynamics (scheme in Fig. 4f). This suggests a direct correlation between the MCD growth (drop) and PL dimming (brightening) due to carrier trapping (detrapping).

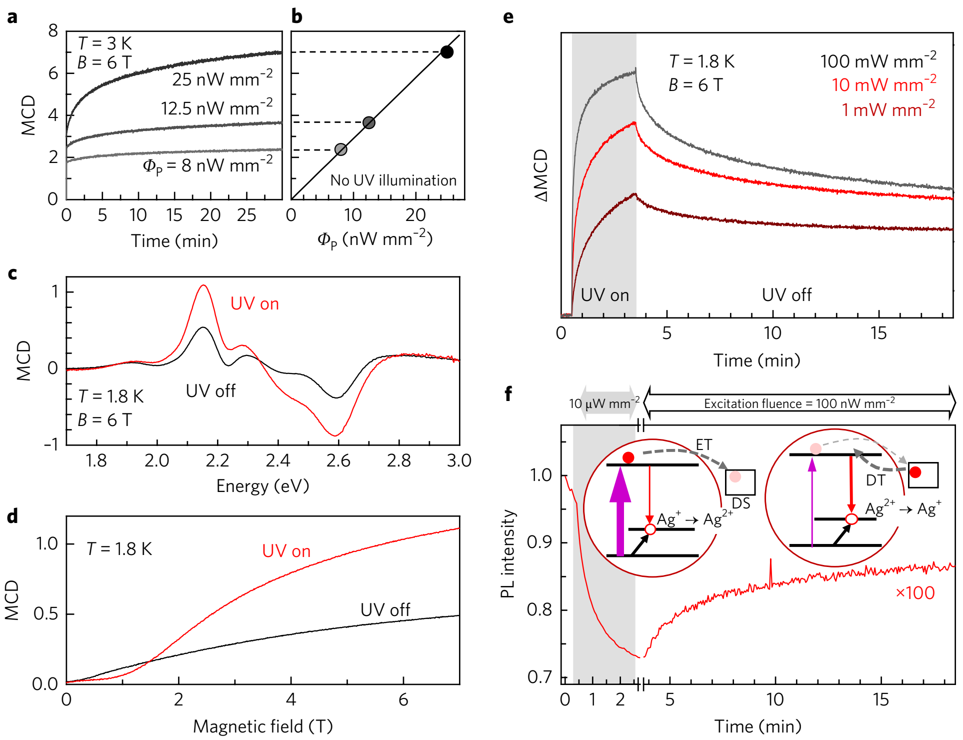

Fig. 4 | Photoinduced paramagnetization of Ag-doped CdSe NCs. a, Evolution of the MCD signal of the 1S exciton of Ag:CdSe NCs over time, measured at 3 K and 6 T using increasingly higher probe fluence. **b**, Linear dependence of MCD intensity on probe intensity (measured after 30 min). **c**, MCD signals measured at constant probe intensity in the presence (red line) and absence (black line) of additional illumination with 3.1 eV UV light (100 μW mm^{-2}). To avoid parasitic heating effects from the UV light source, experiments were performed in superfluid helium at T = 1.8 K, which ensures optimal heat sinking. **d**, Peak MCD signal (measured at 2.15 eV) as a continuous function of applied magnetic field with and without additional UV illumination (100 μW mm^{-2}). **e**, Time evolution of the change in peak MCD signal as additional UV illumination is turned on (grey shading) and off. Stronger UV light leads to larger MCD signal and faster dynamics of both on and off phases. In all cases, the MCD decay is markedly slower than the corresponding rise under UV excitation. **f**, Time evolution of the integrated PL intensity under low or high excitation regimes, corresponding to UV off and on conditions in the MCD scan in **e**. Time axes have the same scale for direct comparison of the similar temporal dynamics, emphasizing the close anticorrelation between the PL intensity and MCD signal. To reproduce the conditions of the MCD scan in the absence of additional UV illumination, we used 3.1 eV light with 100 nW mm^{-2} fluence. The situation in which the sample is exposed to further UV excitation is recreated by increasing the fluence to 10 μW mm^{-2}, corresponding to the laser intensity used in the photoinduced MCD experiments. In all excitation conditions, the excitation rate is well below 10^{-3} excitons per NC, thus excluding multiexcitonic effects. Inset: Schematic depiction of the electron trapping (ET)/detrapping (DT) mechanisms in defect states (DSs) responsible for the ultralong lifetime of the metastable paramagnetic state. Under intense (10 μW mm^{-2}) UV excitation (left scheme), the PL is quenched by ET, which enhances the MCD signal in **d** by favouring the accumulation of photoinduced paramagnetic Ag^{2+} states. When the UV excitation is lowered to 100 nW mm^{-2} (right scheme), slow DT of trapped electrons leads to recovery of the PL signal and a concomitant decrease of MCD intensity.

To experimentally validate this hypothesis, we monitored the PL intensity of the Ag-doped NC film over a timescale analogous to the MCD time trace. Figure 4f shows the remarkable anticorrelation between the PL trend and the MCD time trace in Fig. 4e, with the emission intensity undergoing a relatively faster drop under intense UV excitation due to photocharging by electron trapping, while the MCD signal is concomitantly intensified. Once the excitation fluence is reduced to 100 nW mm^{-2}, the PL intensity slowly recovers on a timescale compatible with the slow decay of the photoinduced MCD. This confirms the assumption that the process responsible for the persistence of the photoinduced magnetism is the slow release of CB electrons trapped in deep acceptor surface states.

Conclusions

In summary, through the combination of optical, SEC and MCD experiments, we have shown that NCs doped with Ag exhibit optically activated paramagnetic properties and concomitant *sp–d* exchange interactions between excitons and Ag dopants, suggesting that optically switchable magnetic nanomaterials can be obtained by exploiting the excitonic processes involving nominally nonmagnetic impurities.

Methods

Methods, including statements of data availability and any associated accession codes and references, are available at https://doi.org/10.1038/s41565-017-0024-8.

Received: 27 July 2017; Accepted: 3 November 2017;
Published online: 18 December 2017

References

1. Pietryga, J. M. et al. Spectroscopic and device aspects of nanocrystal quantum dots. *Chem. Rev.* **116**, 10513–10622 (2016).
2. Sargent, E. H. Colloidal quantum dot solar cells. *Nat. Photon.* **6**, 133–135 (2012).
3. Pelayo García de Arquer, F., Armin, A., Meredith, P. & Sargent, E. H. Solution-processed semiconductors for next-generation photodetectors. *Nat. Rev. Mater.* **2**, 16100 (2017).
4. Medintz, I. L., Uyeda, H. T., Goldman, E. R. & Mattoussi, H. Quantum dot bioconjugates for imaging, labelling and sensing. *Nat. Mater.* **4**, 435–446 (2005).
5. Meinardi, F. et al. Highly efficient luminescent solar concentrators based on earth-abundant indirect-bandgap silicon quantum dots. *Nat. Photon.* **11**, 177–185 (2017).
6. Meinardi, F. et al. Highly efficient large-area colourless luminescent solar concentrators using heavy-metal-free colloidal quantum dots. *Nat. Nanotech.* **10**, 878–885 (2015).

7. Norris, D. J., Efros, A. L. & Erwin, S. C. Doped nanocrystals. *Science* **319**, 1776–1779 (2008).
8. Erwin, S. C. et al. Doping semiconductor nanocrystals. *Nature* **436**, 91–94 (2005).
9. Norris, D. J., Yao, N., Charnock, F. T. & Kennedy, T. A. High-quality manganese-doped ZnSe nanocrystals. *Nano Lett.* **1**, 3–7 (2001).
10. Brovelli, S., Galland, C., Viswanatha, R. & Klimov, V. I. Tuning radiative recombination in Cu-doped nanocrystals via electrochemical control of surface trapping. *Nano Lett.* **12**, 4372–4379 (2012).
11. Sahu, A. et al. Electronic impurity doping in CdSe nanocrystals. *Nano Lett.* **12**, 2587–2594 (2012).
12. Kang, M. S., Sahu, A., Frisbie, C. D. & Norris, D. J. Influence of silver doping on electron transport in thin films of PbSe nanocrystals. *Adv. Mater.* **25**, 725–731 (2013).
13. Ochsenbein, S. T. et al. Charge-controlled magnetism in colloidal doped semiconductor nanocrystals. *Nat. Nanotech.* **4**, 681–687 (2009).
14. Pandey, A. et al. Long-lived photoinduced magnetization in copper-doped ZnSe–CdSe core–shell nanocrystals. *Nat. Nanotech.* **7**, 792–797 (2012).
15. Bussian, D. A. et al. Tunable magnetic exchange interactions in manganese-doped inverted core–shell ZnSe–CdSe nanocrystals. *Nat. Mater.* **8**, 35–40 (2009).
16. Rice, W. D. et al. Revealing giant internal magnetic fields due to spin fluctuations in magnetically doped colloidal nanocrystals. *Nat. Nanotech.* **11**, 137–142 (2016).
17. Rice, W. D. et al. Direct measurements of magnetic polarons in Cd$_{1-x}$Mn$_x$Se nanocrystals from resonant photoluminescence. *Nano Lett.* **17**, 3068–3075 (2017).
18. Muckel, F. et al. Current-induced magnetic polarons in a colloidal quantum-dot device. *Nano Lett.* **17**, 4768–4773 (2017).
19. Krustok, J., Mädasson, J., Altosaar, M. & Kukk, P. The nature of recombination centres in silver- and chlorine-doped CdS phosphors. *J. Phys. Chem. Solids* **51**, 1013–1018 (1990).
20. Krustok, J. Orange luminescence of donor–acceptor pairs in CdS:Ag:Cl. *J. Phys. Chem. Solids* **53**, 1027–1030 (1992).
21. Peka, P. & Schulz, H.-J. Empirical one-electron model of optical transitions in Cu-doped ZnS and CdS. *Phys. B* **193**, 57–65 (1994).
22. Stringfellow, G. B. & Bube, R. H. Photoelectronic properties of ZnSe crystals. *Phys. Rev.* **171**, 903–915 (1968).
23. Viswanatha, R., Brovelli, S., Pandey, A., Crooker, S. A. & Klimov, V. I. Copper-doped inverted core/shell nanocrystals with 'permanent' optically active holes. *Nano Lett.* **11**, 4753–4758 (2011).
24. Nelson, H. D. et al. Mid-gap states and normal vs inverted bonding in luminescent Cu$^+$- and Ag$^+$-doped CdSe nanocrystals. *J. Am. Chem. Soc.* **139**, 6411–6421 (2017).
25. Liu, J. et al. Heterovalent-doping-enabled efficient dopant luminescence and controllable electronic impurity via a new strategy of preparing II–VI nanocrystals. *Adv. Mater.* **27**, 2753–2761 (2015).
26. Mocatta, D. et al. Heavily doped semiconductor nanocrystal quantum dots. *Science* **332**, 77–81 (2011).
27. Kompch, A. et al. Localization of Ag dopant atoms in CdSe nanocrystals by reverse Monte Carlo analysis of EXAFS spectra. *J. Phys. Chem. C* **119**, 18762–18772 (2015).
28. Grochala, W. & Hoffmann, R. Real and hypothetical intermediate-valence Ag^{II}/Ag^{III} and Ag^{II}/Ag^{I} fluoride systems as potential superconductors. *Angew. Chem. Int. Ed.* **40**, 2742–2781 (2001).
29. Dean, P. J., Fitzpatrick, B. J. & Bhargava, R. N. Optical properties of ZnSe doped with Ag and Au. *Phys. Rev. B* **26**, 2016–2035 (1982).
30. Holtz, P. O., Monemar, B. & Loykowski, H. J. Optical properties of Ag-related centers in bulk ZnSe. *Phys. Rev. B* **32**, 986–996 (1985).
31. Nedeoglo, N. D., Sirkeli, V. P., Nedeoglo, D. D., Laiho, R. & Lähderanta, E. Electron configuration and charge state of electrically active Cu, Ag and Au ions in ZnSe. *J. Phys. Condens. Matter* **18**, 8113 (2006).
32. McMillan, J. A. Higher oxidation states of silver. *Chem. Rev.* **62**, 65–80 (1962).
33. Burdett, J. K. & Eisenstein, O. From three- to four-coordination in copper(I) and silver(I). *Inorg. Chem.* **31**, 1758–1762 (1992).
34. Vydyanath, H. R. & Kröger, F. A. The defect structure of silver-doped CdS. *J. Phys. Chem. Solids* **36**, 509–520 (1975).
35. Jana, S., Manna, G., Srivastava, B. B. & Pradhan, N. Tuning the emission colors of semiconductor nanocrystals beyond their bandgap tunability: all in the dope. *Small* **9**, 3753–3758 (2013).
36. Srivastava, B. B., Jana, S. & Pradhan, N. Doping Cu in semiconductor nanocrystals: some old and some new physical insights. *J. Am. Chem. Soc.* **133**, 1007–1015 (2011).
37. Lupo, M. G. et al. Ultrafast electron–hole dynamics in core/shell CdSe/CdS dot/rod nanocrystals. *Nano Lett.* **8**, 4582–4587 (2008).
38. Pinchetti, V. et al. Spectro-electrochemical probing of intrinsic and extrinsic processes in exciton recombination in I–III–VI$_2$ nanocrystals. *Nano Lett.* **17**, 4508–4517 (2017).
39. Lorenzon, M. et al. Role of nonradiative defects and environmental oxygen on exciton recombination processes in CsPbBr$_3$ perovskite nanocrystals. *Nano Lett.* **17**, 3844–3853 (2017).
40. Lorenzon, M. et al. Reversed oxygen sensing using colloidal quantum wells towards highly emissive photoresponsive varnishes. *Nat. Commun.* **6**, 6434 (2015).
41. Padilha, L. A. et al. Spectral dependence of nanocrystal photoionization probability: the role of hot-carrier transfer. *ACS Nano* **5**, 5045–5055 (2011).
42. Furdyna, J. K. Diluted magnetic semiconductors. *J. Appl. Phys.* **64**, R29–R64 (1988).
43. Kuno, M., Nirmal, M., Bawendi, M. G., Efros, A. & Rosen, M. Magnetic circular dichroism study of CdSe quantum dots. *J. Chem. Phys.* **108**, 4242–4247 (1998).
44. Schulz, H. J. Optical properties of 3*d* transition metals in II–VI compounds. *J. Cryst. Growth* **59**, 65–80 (1982).
45. Schulz, H. J. Transition metal impurities in compound semiconductors: experimental situation. *Mater. Chem. Phys.* **16**, 373–384 (1987).
46. Johnston-Halperin, E. et al. Spin spectroscopy of dark excitons in CdSe quantum dots to 60 T. *Phys. Rev. B* **63**, 205309 (2001).
47. Stern, N. P. et al. Spin dynamics in electrochemically charged CdSe quantum dots. *Phys. Rev. B* **72**, 161303 (2005).
48. Archer, P. I., Santangelo, S. A. & Gamelin, D. R. Direct observation of *sp*–*d* exchange interactions in colloidal Mn^{2+}- and Co^{2+}-doped CdSe quantum dots. *Nano Lett.* **7**, 1037–1043 (2007).
49. Poolton, N. R. J., Davies, J. J., Nicholls, J. E. & Fitzpatrick, B. J. An ODMR investigation of silver doped ZnSe. *J. Cryst. Growth* **72**, 336–341 (1985).

Acknowledgements

Q.D. and J.Z. acknowledge support from the National Natural Science Foundation of China (grants 51372025, 91323301 and 51631001). A.C. and M.Z.-R. acknowledge support from the project MIUR-PRIN 2015WTW7J3. Work at the National High Magnetic Field Laboratory is supported by the US National Science Foundation (DMR-1157490), the State of Florida, and the US Department of Energy.

Author contributions

S.B. conceived this study. Q.D. and J.Z. developed and synthesized the samples and performed the structural and analytical characterization. V.P. and M.L., with the assistance of M.F. and F.M., performed the optical and spectroelectrochemical measurements. A.C., V.P. and M.Z.-R. collected and analysed the transient transmission data. V.P. and S.A.C. performed the magneto-optical experiments. V.P., S.A.C. and S.B. analysed the data. V.P. and S.B. wrote the paper in consultation with all authors.

Competing interests

The authors declare no competing financial interests.

Additional information

Supplementary information is available for this paper at https://doi.org/10.1038/s41565-017-0024-8.

Reprints and permissions information is available at www.nature.com/reprints.

Correspondence and requests for materials should be addressed to J.Z. or S.B.

Methods

Synthesis of Ag-doped CdSe NCs. For synthesis of the 3% Ag-doped CdSe NCs (~5 nm), CdSe NCs were synthesized via the in situ sulfuration and cation exchange reaction of Ag nanoparticles (NPs). Monodisperse Ag NPs (~5 nm) were prepared first, according to the methods of ref. [50], for further use in the preparation of amorphous Ag_2Se NPs by reaction with a Se precursor in the molar ratio 1:5 at 50 °C. The Se precursor was prepared from 1 mmol Se powder with 7 ml octadecylene at 270 °C. The obtained Ag_2Se NCs (0.035 mmol) were dispersed in 10 ml toluene with 0.2 ml oleic acid (OA) and 0.1 ml oleylamine (OAm), then a 1 ml methanol solution containing 0.1 g $Cd(NO_3)_2{\cdot}4H_2O$ was added. After 2 min magnetic stirring, 0.1 ml tributylphosphine (TBP) was added, and the mixture was heated at 55 °C for 1 h under magnetic stirring.

Film preparation. Optical-quality NC films were essential for clean MCD data. To produce low-scattering NC films, 4 ml NCs in $CHCl_3$ was added dropwise to 5 ml of continuously stirred 2% (wt/wt) polyvinylpyrrolidone (PVP) in $CHCl_3$. This mixture was then transferred to a centrifuge tube where hexane was added to precipitate out the NC-PVP solids. The sample was then centrifuged at 5,000 r.p.m. for 5 min, producing a dense sedimented pellet and a clear supernatant at the top, which was discarded. The pellet was redissolved by sonication with 600 µl of 1% PVP in 20% wt/wt butanol/chloroform. A 200 µl volume of this viscous liquid was spread on a 25 mm square glass coverslip, and then spun at 500 r.p.m. for 120 s followed by an additional 60 s at 2,000 r.p.m. The resulting films were ~20 µm thick and exhibited good optical uniformity and low scattering.

Structural characterization. Samples for TEM characterization were prepared by placing one drop of toluene solution, together with the product, onto a 300-mesh copper grid with a carbon support film. A JEOL JEM 1200EX transmission electron microscope (TEM) working at 100 kV and a high-resolution (HR) TEM (FEI Tecnai G2 F20 S-Twin) working at 200 kV were utilized to characterize the morphology of the CdSe NCs. X-ray photoelectron spectroscopy (XPS) spectra were obtained with a PHI Quantera II X-ray photoelectron spectrometer using Al Kα non-monochromatic radiation. The colloidal NPs were dip-coated on a silicon substrate for XPS characterization with the following measurement parameters: light spot size, 100 µm; power, 100 W; voltage, 20 kV. An energy correction was made to account for sample charging based on the C1*s* peak at 284.8 eV. The elemental concentrations listed in Supplementary Table 1 are reported relative to carbon, calculated from the XPS spectra based on the area of the characteristic photoelectron peaks after correcting for atomic sensitivity. The estimated average number of Ag atoms per NC, extracted from the data in Supplementary Table 1, is $N_{Ag} = 49 \pm 8$ (expected value ± standard deviation). Under these conditions, no undoped NCs are statistically expected in the ensemble.

Spectroscopic studies. Absorption spectra were recorded using a Varian Cary 50 spectrophotometer. PL measurements were performed using a pulsed diode laser at 3.1 eV (Edinburgh Inst. EPL 405, 40 ps pulse width) as the excitation source and collecting the emitted light with a TM-C10083CA Hamamatsu Mini-Spectrometer. Time-resolved PL experiments were conducted using the same excitation source and collecting with a Hamamatsu R943-02 time-correlated single-photon counting unit coupled to an Oriel Instruments Cornerstone 260 monochromator. All PL measurements were performed with a power density of 100 nJ cm^{-2}. For PL excitation and PL experiments under resonant excitation conditions, a spectrally narrow photoexcitation source (<0.5 nm full-width at half-maximum) was produced by filtering the output of a 150 W xenon lamp with a 1/3 m double-grating Gemini monochromator. The emitted PL was collected with a Horiba Scientific Triax 180 1/2 m spectrograph and detected with an Instruments SA Spectrum One liquid-nitrogen-cooled charge-coupled device. All measurements were carried out at room temperature except the photocharging experiments, which were conducted at 18 K.

Transient transmission spectroscopy. For the ultrafast transient transmission measurements, the laser source was a Ti:sapphire laser with chirped pulse amplification (Coherent LIBRA-HE), which provided 95 fs pulses at 800 nm at a repetition rate of 2 kHz. The excitation pulses at 2.3 eV (540 nm) and 1.95 eV (635 nm) were generated with an optical parametric amplifier. The bandwidth of the pump pulses was 10 nm, corresponding to a pulse duration ~100 fs. The probe beam was a white-light supercontinuum generated by focusing a small fraction of the fundamental beam onto a 2-mm-thick sapphire plate. The supercontinuum spectrum extended from 450 nm to 1.6 µm, with a gap only around the fundamental wavelength at 800 nm. Pump and probe were then focused on the sample by means of a lens and a spherical mirror. Pump fluences in the position of the white light focus were on the order of 35 µJ cm^{-2} and 95 µJ cm^{-2} for 2.3 eV and 1.95 eV pump, respectively.

A computer-controlled optical multichannel analyser working at 1 kHz was used to acquire the map of the differential transmission $\Delta T/T = (T_{on} - T_{off})/T_{off}$, as a function of the pump–probe time delay, where T_{on} and T_{off} are the probe spectra transmitted by the excited and unperturbed samples, respectively. In data analysis, we neglected the spectral region near the pump beams (0.6–0.7 eV around the peaks).

SEC measurements. ITO-coated glass slides (50 × 7 × 0.7 mm, $R_S < 100\,\Omega$) were purchased from Delta Technologies (part no. CG-90IN-CUV). The ITO-coated surface was first covered with ZnO NPs (Nanograde, ~50 nm diameter) to avoid quenching of NC emission by fast charge/energy transfer to the ITO. The ZnO NP layer (~60 nm thick, measured using a Dektak profilometer) was deposited by dip-coating the glass/ITO substrate into an ethanol suspension of ZnO NPs (2 mg ml^{-1}, one dip for 10 s) and annealed at 150 °C for 10 min in a nitrogen glovebox. To test the stability of the glass/ITO/ZnO NP substrates during potential scans, we performed control experiments in which we monitored changes in optical absorption spectra for prolonged exposures to negative and positive potentials. The results of these measurements indicate that the substrates are unaffected by either positive or negative EC potentials for exposure times of tens of minutes, which are much longer than the measurement time used in our SEC experiments (~10 min). The NCs were deposited onto the ZnO NP layer as a few-monolayer-thick film by dip-coating from a dilute toluene solution (optical density of 0.07 at 500 nm; two dips for 10 s). The ZnO NP layer used in this study was not treated with crosslinkers and therefore it represented a dielectric tunnelling barrier of ~1 V. The introduction of the additional ZnO spacer as well as the presence of insulating surface ligands can also lead to an appreciable attenuation of the actual shift of the FL compared to the nominal applied EC potential. The ITO was connected as a working electrode to the potentiostat (Bio Logic SP-200 Research grade potentiostat/galvanostat) and the film was placed into a quartz cuvette filled with the electrolyte (0.1 M tetrabutylammonium perchlorate ($TBAClO_4$) in propylene carbonate). Ag and Pt wires were used as quasi-reference and counter electrodes, respectively. All potentials reported in this work were measured relative to the quasi-reference Ag electrode during staircase voltammetry scans (10 s scan rate). The film was excited at 3.1 eV with continuous-wave diode lasers and the emitted light was collected with a focusing lens and sent to a spectrometer coupled to a USB4000 Ocean Optics spectrometer.

MCD measurements. We used standard MCD methods[43] to measure the field- and temperature-dependent Zeeman splitting (ΔE_Z) of the 1S exciton absorption resonance in our NCs, from which the presence of any additional *sp*–*d* exchange coupling of the exciton to paramagnetic dopants can be inferred. As in conventional diluted magnetic semiconductors[42], paramagnetic moments in the NC are revealed via an enhanced and strongly temperature-dependent ΔE_Z. MCD measures, as a function of photon energy, the (normalized) difference in transmission between right and left circularly polarized light through the NC film in the Faraday geometry, $(T_R - T_L)/(T_R + T_L)$ (ref. [15]). When the Zeeman splitting is small compared to the width of the 1S exciton absorption (as is the case here), the MCD spectrum is therefore derivative-like with a low-energy maximum proportional to ΔE_Z. NC films were mounted in the variable-temperature insert (1.5–300 K) of a 7 T superconducting magnet with direct optical access. Probe light of tunable wavelength was derived from a xenon lamp directed through a spectrometer. The probe light was mechanically chopped at 137 Hz, and was modulated between right and left circular polarizations at 50 kHz using a photoelastic modulator. The transmitted light was detected with a silicon avalanche photodiode. Photomagnetization was induced with additional light from a continuous-wave 3.1 eV diode laser.

Data availability. The data that support the plots within this paper and other findings of this study are available from the corresponding author upon reasonable request.

References

50. Li, L., Hu, F., Xu, D., Shen, S. & Wang, Q. Metal ion redox potential plays an important role in high-yield synthesis of monodisperse silver nanoparticles. *Chem. Commun.* **48**, 4728–4730 (2012).